

## Vicarious calibration of EO-1 Hyperion

Journal:	<i>Journal of Selected Topics in Applied Earth Observations and Remote Sensing</i>
Manuscript ID:	JSTARS-2012-00067
Manuscript type:	The Earth Observing One (EO-1) Satellite Mission: Over a Decade in Space Special Issue
Date Submitted by the Author:	29-Feb-2012
Complete List of Authors:	McCorkel, Joel; NASA, Biospheric Sciences Thome, Kurt; NASA, Biospheric Sciences Ong, Lawrence; Science Systems and Applications, Inc., NASA/GSFC
Keywords:	Calibration

SCHOLARONE™  
Manuscripts

Only

## Vicarious calibration of EO-1 Hyperion

Joel McCorkel, Kurtis Thome, Lawrence Ong

### Abstract

The Hyperion imaging spectrometer on the Earth Observing-1 satellite is the first high-spatial resolution imaging spectrometer to routinely acquire science-grade data from orbit. Data gathered with this instrument needs to be quantitative and accurate in order to derive meaningful information about ecosystem properties and processes. Also, comprehensive and long-term ecological studies require these data to be comparable over time, between coexisting sensors and between generations of follow-on sensors. One method to assess the radiometric calibration is the reflectance-based approach, a common technique used for several other earth science sensors covering similar spectral regions. This work presents results of radiometric calibration of Hyperion based on the reflectance-based approach of vicarious calibration implemented by University of Arizona during 2001–2005. These results show repeatability to the 2% level and accuracy on the 3–5% level for spectral regions not affected by strong atmospheric absorption. Knowledge of the stability of the Hyperion calibration from moon observations allows for an average absolute calibration based on the reflectance-based results to be determined and applicable for the lifetime of Hyperion.

### I. Introduction

Over a decade of measurements made by the Hyperion imaging spectrometer has enabled scientists to explore new methods and algorithms of characterizing the earth's surface with high spectral fidelity remote sensing data. Many of these and future techniques use physics-based calculations to extract land-use and land-cover changes, biochemical and biophysical properties of the earth's surface from Hyperion's imagery. For this, and to allow consistency with current and future remote sensing instrumentation, accurate and traceable calibration is required.

There are many techniques to ensure that a sensor's calibration is known and each has its own strengths and weaknesses. Preflight characterization is the most thorough but it is often difficult to create test apparatus that exactly emulate operational conditions and anticipate how the sensor may be affected by launch and the space environment (Barnes et

1  
2  
3 al, 2001). Many sensors, including Hyperion, have on-board calibrators that provide  
4  
5 valuable information about sensor behavior such as detector-to-detector variability and  
6  
7 trends in sensor health. However, on-board calibrators will never be able to provide an  
8  
9 absolute calibration that is more accurate than the preflight characterization.  
10  
11

12  
13 Several techniques have been developed to characterize sensors vicariously and  
14  
15 independent from prelaunch and on-board calibrators including repeated lunar  
16  
17 acquisitions, comparisons to other sensors, and comparisons to ground-based  
18  
19 measurements. Distinct advantages of the moon look technique is that the surface of the  
20  
21 moon is highly stable and provides a data set with reasonable temporal frequency that  
22  
23 will improve over time as the knowledge of the lunar phase effects becomes more  
24  
25 accurate and precise. Comparisons with other sensors, also referred to as cross-calibration  
26  
27 or inter-comparison, is complex due to variables such as coincident acquisition times,  
28  
29 viewing and illumination geometries, and spectral coverage differences. These issues are  
30  
31 compounded when transferring calibration knowledge from one sensor to another and  
32  
33 this technique can only be as accurate as the sensor's prelaunch characterization. The  
34  
35 third method mentioned uses ground-based measurements to predict the sensor's  
36  
37 calibration.  
38  
39  
40  
41  
42

43  
44 Ideally, all of these calibration techniques would be implemented for Hyperion  
45  
46 and all would agree within their uncertainties. Unfortunately, it was found that the  
47  
48 radiometric response of Hyperion changed significantly between preflight  
49  
50 characterization and early on-orbit results in 2001 (Biggar et al, 2003). Subsequent  
51  
52 imagery from Hyperion included approximately 10% and 20% spectrally flat factors on  
53  
54 radiance for the VNIR and SWIR focal planes, respectively. This work provides a more  
55  
56  
57  
58  
59  
60

1  
2  
3 accurate and spectrally dependent radiometric characterization for Hyperion using a  
4 combination of vicarious techniques. First, the reflectance-based approach is used to find  
5  
6 the absolute radiometric calibration and, second, historical lunar acquisitions are used to  
7  
8 show that it is valid throughout most of the sensor's lifetime.  
9  
10

11  
12 The next section describes the reflectance-based approach including test sites  
13 employed, measurement techniques, prediction of at-sensor radiance and formulation of  
14  
15 results followed by discussion of lunar acquisitions and the long-term stability of  
16  
17 Hyperion. The third section presents results based on field measurements collected 2001–  
18  
19 2005 with supporting moon-based studies. The reflectance-based and moon-based results  
20  
21 are used in combination to provide an absolute radiometric calibration and show that it is  
22  
23 valid 2001–present. The final section discusses limitations of results presented here  
24  
25 regarding the spatial channels for which this work is valid and provides direction for  
26  
27 future work that extends these results to the entire focal plane.  
28  
29  
30  
31  
32  
33  
34  
35  
36  
37  
38

## 39 **II. Reflectance-based approach**

40  
41  
42 One method of vicarious validation of at-sensor radiance is the reflectance-based  
43  
44 approach, successfully implemented by several research groups and applied to dozens of  
45  
46 Earth-observing sensors (Vane et al, 1993; Thome, 2001; Thome, 2004a,b; Arai et al,  
47  
48 2005). This method relies on in situ measurements that characterize surface reflectance  
49  
50 and atmospheric properties of a test site to provide input to a radiative transfer model to  
51  
52 predict at-sensor radiance. These values are then compared with corresponding  
53  
54  
55  
56  
57  
58  
59  
60

1  
2  
3 measurements of the airborne or spaced-based sensor. The remainder of this section  
4  
5 describes the approach for each of these aspects.  
6  
7  
8  
9

### 10 *A. Test site*

11  
12  
13  
14  
15 Desirable test site properties for the reflectance-based approach as well as other  
16  
17 calibration methods include high-reflectance, spatially uniform over large areas, and high  
18  
19 in elevation (Scott et al., 1996). The overarching idea behind these characteristics is to  
20  
21 get closer to the ideal case of zero atmosphere by maximizing the signal due to directly  
22  
23 reflected solar irradiance. A bright test site with a reflectance with 0.3 or greater  
24  
25 maximizes signal component due to directly reflected solar irradiance for most spectral  
26  
27 regions. Spatially uniform sites reduce concerns such as registration and adjacency  
28  
29 effects seen in some radiative transfer studies when the surface reflectance surrounding  
30  
31 the test site is different than that of the test site. Test sites at high elevations have less  
32  
33 atmospheric aerosols and errors associated with their characterization have less effect.  
34  
35 Other desirable test site characteristics are near lambertian reflectance properties and  
36  
37 temporal stability. A lambertian site will reduce effects due to solar and view geometries.  
38  
39 A temporally stable site allows consistency between day-to-day, season-to-season, and  
40  
41 year-to-year studies. Lastly, logistics and cost of traveling to a test site with an assortment  
42  
43 of personnel and instrumentation control the locality of the test site. The Railroad Valley  
44  
45 Playa (RVPN), a large desert basin in Nevada, satisfactorily satisfies the criteria  
46  
47 described above and is selected for this work.  
48  
49  
50  
51  
52  
53  
54  
55  
56  
57  
58  
59  
60

1  
2  
3  
4  
5  
6  
7  
8  
9  
10  
11  
12  
13  
14  
15  
16  
17  
18  
19  
20  
21  
22  
23  
24  
25  
26  
27  
28  
29  
30  
31  
32  
33  
34  
35  
36  
37  
38  
39  
40  
41  
42  
43  
44  
45  
46  
47  
48  
49  
50  
51  
52  
53  
54  
55  
56  
57  
58  
59  
60

This work includes two rectangular test site layouts used at RVPN: a  $90 \times 240$  meter site with its long edge in Hyperion's cross-track direction and a  $120 \times 480$  meter site with its short edge in Hyperion's cross-track direction. Considering that Hyperion has a 30-meter ground sample distance, these sites represent 8 and 4 spatial pixels in Hyperion's cross-track, respectively. Earlier data sets use the site orientation that cover more of the cross-track pixels due to a focused effort to characterize EO-1 sensors during its first year of operation. Later data sets use the  $120 \times 480$  meter site optimized for a Landsat-type sensor (Thome, 2001).

### ***B. Reflectance characterization***

In most spectral regions in the solar-reflective spectrum, the dominant signal component is directly reflected solar irradiance and therefore surface reflectance characterization is the most important aspect of the reflectance-based approach. The following method characterizes the biconical reflectance factor of the test site for the geometry given by the solar position and the view of ground-based instrument. Biconical reflectance is the measured quantity, however this will be approximated as the bidirectional reflectance factor (BRF) in this work due to the small angular subtense of source and sensor. Also, the solar geometry changes throughout the period of the measurement meaning the ground-based BRF measurement is not exactly the same as the BRF conditions at the time that the sensor acquired the test site. Near-Lambertian test sites and measuring the surface reflectance close in time to the sensor acquisition reduces errors associated with geometry effects.

1  
2  
3 The  $90 \times 240$  and  $120 \times 480$  meter sites are sampled over evenly spaced transects.  
4  
5 For a reasonably uniform site transect spacing is selected to be the ground-sample  
6  
7 distance of the imager; more frequent spacing may increase sampling time too much and  
8  
9 less frequent spacing may not provide enough statistical sampling for each detector.  
10  
11

12  
13 Measurements obtained by a field-portable spectroradiometer are used to  
14  
15 calculate the reflectance of the test site. These measurements consist of a 16-bit output at  
16  
17 1-nm spectral intervals covering a spectral range of 350–2500 nm. The 1-nm interval data  
18  
19 is interpolated from raw measurements of 1.4 nm sampling intervals with 3-nm resolution  
20  
21 from 350-1000 nm and 2-nm sampling intervals with 10 nm resolution from 1000–2500  
22  
23 nm. Light is gathered by a fiber optic bundle that feeds the entrance slit of the  
24  
25 spectroradiometer. The 25-degree field-of-view of the fiber optic bundle is converted to 8  
26  
27 degrees with a foreoptic giving the instrument a footprint of about 20 cm when held at  
28  
29 about 1.5 m above the ground. The instrument is carried by an operator along each of the  
30  
31 transects mentioned above. A reference measurement is taken over a well-characterized  
32  
33 diffuser before and after each transect.  $BRF(0^\circ, \theta)$  of the diffuser traceable to standards  
34  
35 defined by National Institute of Standards and Technology (NIST) is characterized in five  
36  
37 degree increments of  $\theta$  in the range of possible solar geometries over the 350–2500 nm  
38  
39 spectral region in 22 narrow spectral bands (Biggar et al, 1988). Using reference  
40  
41 measurements surrounding each of the test site transect measurements and their  
42  
43 associated timestamps, automated processing techniques calculate a reference BRF for  
44  
45 each measurement along the transect to compensate for varying solar illumination  
46  
47 geometries throughout the duration of measurements. The calculated reference BRF  
48  
49 values are transferred to each of the transect measurements providing NIST-traceable  
50  
51  
52  
53  
54  
55  
56  
57  
58  
59  
60

1  
2  
3 BRF of the test site. The mean of these spectral BRF values are used to constrain the  
4  
5 radiative transfer model.  
6  
7  
8  
9

#### 10 ***D. Atmospheric characterization***

11  
12  
13  
14  
15 Although directly reflected radiance is the dominant part of the at-sensor signal for the  
16  
17 bright surface and high elevation of RVPN, atmospheric effects must be considered to  
18  
19 accurately predict at-sensor radiance. Molecular and aerosol components of the  
20  
21 atmosphere attenuate and scatter light with strong spectral dependencies. Characterizing  
22  
23 these effects relies on atmospheric temperature and pressure measurements and solar  
24  
25 extinction measurements from a ten spectral channel solar radiometer. The effects of the  
26  
27 molecular component are characterized using the Rayleigh approximation using  
28  
29 atmospheric temperature and pressure data (Penndorf 1957, Teillet 1990). Next, effects of  
30  
31 the aerosol component and absorption features are characterized using atmospheric  
32  
33 optical depths retrieved from solar radiometer measurements that are relatively calibrated  
34  
35 using the Langley method (Biggar, 1990; Gellman et al., 1991). Columnar ozone amount  
36  
37 is extracted from a freely available database of total ozone derived from measurements  
38  
39 by either Total Ozone Mapping Spectrometer (TOMS) or Ozone Monitoring Instrument  
40  
41 (OMI) depending on the date (McPeters et al., 1998; Veefkind et al., 2006). A power law  
42  
43 is used to describe the aerosol size distribution and to derive at values for aerosol optical  
44  
45 depth at 1-nm intervals over the 350–2500 nm spectral range (Ångström, 1929). Lastly,  
46  
47 columnar water vapor is derived from the solar radiometer measurements using a  
48  
49 modified Langley approach (Reagan et al., 1992).  
50  
51  
52  
53  
54  
55  
56  
57  
58  
59  
60



### *E. Radiative transfer*

The surface and atmospheric properties found above serve to constrain the radiative transfer code that predicts at-sensor radiance for a variety of remote sensing instrumentation. The code used in this work is MODTRAN4 (Berk et al., 1987; Berk et al., 1998). The model assumes a solar spectrum, the Chance-Kurucz curve for this work, and simulates its path through the atmosphere to the ground, its interaction with the ground, and finally its path towards the sensor. The bottom layer is Earth's surface and is modeled to be opaque and characterized by the input reflectance spectrum. Transmittance calculations are based on band models of molecular line absorption, continuous molecular absorption, and extinction coefficients of aerosols.

Geometries of the sensor and sun at the time the sensor measures the test site are also included in the input. The mid-latitude summer atmospheric model in MODTRAN is used in this work which defines atmospheric profiles for H<sub>2</sub>O, O<sub>3</sub>, N<sub>2</sub>O, CO, and CH<sub>4</sub> that are proper for the altitude, pressure and column ozone provided to the model. The CO<sub>2</sub> mixing ratio is set to 365 ppm. Aerosol optical depth at 550 nm and Ångström parameter is provided to define aerosol spectral extinction. The size distribution derived from the solar radiometer measurements using power law assumption is used to Mie scattering spectral phase functions.

The model is set to assume a lambertian surface with spectral reflectance of the test site that is measured close in time to sensor acquisition. This assumption is valid if geometries of ground-based measurements match those of the remote sensing instrument

1  
2  
3 (i.e. the foreoptic of the field-portable spectroradiometer is pointing at the test site in the  
4 same direction as the remote sensing instrument). The model assumes that the entire  
5 surface has the same reflectance, which may cause inaccurate results if the area  
6 surrounding the test site has significantly different spectral reflectance due to ground-  
7 atmosphere interaction. Due to the large area of RVPN (approximately  $15 \times 20$  km) and  
8 its typical low aerosol loading, the atmospheric point-spread function drops substantially  
9 outside of the test sites used in this work.  
10  
11  
12  
13  
14  
15  
16  
17  
18  
19

20 The output of MODTRAN provides at-sensor radiance at 1-nm intervals with slit  
21 functions of 2-nm full-width at half maximum. These data are band-averaged with the  
22 appropriate relative spectral responses of Hyperion.  
23  
24  
25  
26  
27  
28

### 29 ***F. Determination of sensor-reported radiance***

30  
31  
32  
33

34 At-sensor radiance calculated using surface reflectance characterization, derived  
35 atmospheric properties, and solar and view geometries is compared with that measured  
36 by Hyperion therefore providing validation independent of laboratory- and onboard-  
37 based characterizations. The radiance values representing the test site reported by the  
38 sensor are determined by extracting the pixel values that represent the test site. To assist  
39 in finding the test site in the imagery blue-colored tarpaulins are deployed on the  
40 southwest corner of the site. Each spatial column of Hyperion has slightly different  
41 spectral characteristics than adjacent columns since it is a pushbroom spectrometer. This  
42 means that each pixel of Hyperion has a unique spectral response function, the case for  
43 all imaging spectrometers. Prelaunch characterization showed that Hyperion's spectral  
44  
45  
46  
47  
48  
49  
50  
51  
52  
53  
54  
55  
56  
57  
58  
59  
60

1  
2  
3 response functions are well represented with gaussian functions and therefore only center  
4 wavelength and full-width at half-maximum values are needed to fully define the spectral  
5 response of each pixel. Variation in spectral response function varies slowly such that  
6 there is small change over the extent of a few pixels but larger differences are seen from  
7 different locations on the focal plane. Each instance of reflectance-based calibration  
8 covers a different group of spatial columns of Hyperion. Spatial column information is  
9 recorded when extracting sensor-reported radiance from Hyperion imagery to accurately  
10 account for varying spectral properties across the spatial swath.  
11  
12  
13  
14  
15  
16  
17  
18  
19  
20  
21  
22  
23  
24  
25  
26  
27  
28  
29  
30  
31

### 32 **III. Hyperion lunar acquisitions and comparison to ROLO**

33  
34  
35

36 The moon is a convenient calibration source for remote sensing systems because  
37 it meets the ideal case of an atmosphere-free surface and has a temporally-stable surface,  
38 that is reasonably bright, and illuminated with the same solar source as the earth (Kieffer  
39 and Wildley, 1996). Research groups have measured the moon over time and over many  
40 spectral channels (Kieffer and Stone, 2005). This work compares the calibration of  
41 Hyperion to that of the U.S. Geological Survey Robotic Lunar Observatory (ROLO)  
42 model (Stone et al., 2003). Inputs to the ROLO model include moon disk-integrated lunar  
43 spectral irradiance, time of observation, position of spacecraft, and size of lunar images in  
44  
45  
46  
47  
48  
49  
50  
51  
52  
53  
54  
55  
56  
57  
58  
59  
60

1  
2  
3 the along-track direction. The precision of the ROLO model allow instruments to track  
4 changes at the 0.1% level (Stone and Kieffer, 2004; Keiffer and Stone, 2005).  
5  
6  
7

8 EO-1 typically collects Hyperion full lunar disk images every two months to  
9 supplement trending of the instrument's performance. These are conducted when the  
10 spacecraft is in the earth's shadow and when the moon phase angle with respect to the  
11 earth of about 7.5 degrees. The data collected are radiometrically corrected and the total  
12 irradiances of the moon for each band are calculated from these Level-1R images. The  
13 ROLO model is used as a basis for normalizing the measured irradiance to account for  
14 the effects of lunar nutation, libration and variances of the sun-moon and moon-  
15 spacecraft ranges.  
16  
17  
18  
19  
20  
21  
22  
23  
24  
25  
26  
27  
28

#### 29 **IV. Results**

30  
31  
32  
33  
34 The reflectance-based approach of vicarious absolute calibration was successfully  
35 implemented nine times for Hyperion using the Railroad Valley Playa test site in Nevada.  
36 These results were obtained over the 2001–2005 period while the EO-1 spacecraft shared  
37 a similar orbit with Landsat 7 making ground validations efforts convenient by sharing  
38 data sets with multiple satellite sensors. After 2005 the orbit of EO-1 changed, limited  
39 resources prevented exclusive campaigns for the sensors of EO-1. Fortunately, EO-1 has  
40 routinely made measurements of the moon beginning shortly after its launch. This section  
41 presents results from the reflectance-based approach and lunar acquisitions that when  
42 combined give a radiometric characterization valid for nearly the entire lifetime of  
43  
44  
45  
46  
47  
48  
49  
50  
51  
52  
53  
54  
55  
56  
57  
58  
59  
60  
61  
62  
63  
64  
65  
66  
67  
68  
69  
70  
71  
72  
73  
74  
75  
76  
77  
78  
79  
80  
81  
82  
83  
84  
85  
86  
87  
88  
89  
90  
91  
92  
93  
94  
95  
96  
97  
98  
99  
100  
101  
102  
103  
104  
105  
106  
107  
108  
109  
110  
111  
112  
113  
114  
115  
116  
117  
118  
119  
120  
121  
122  
123  
124  
125  
126  
127  
128  
129  
130  
131  
132  
133  
134  
135  
136  
137  
138  
139  
140  
141  
142  
143  
144  
145  
146  
147  
148  
149  
150  
151  
152  
153  
154  
155  
156  
157  
158  
159  
160  
161  
162  
163  
164  
165  
166  
167  
168  
169  
170  
171  
172  
173  
174  
175  
176  
177  
178  
179  
180  
181  
182  
183  
184  
185  
186  
187  
188  
189  
190  
191  
192  
193  
194  
195  
196  
197  
198  
199  
200  
201  
202  
203  
204  
205  
206  
207  
208  
209  
210  
211  
212  
213  
214  
215  
216  
217  
218  
219  
220  
221  
222  
223  
224  
225  
226  
227  
228  
229  
230  
231  
232  
233  
234  
235  
236  
237  
238  
239  
240  
241  
242  
243  
244  
245  
246  
247  
248  
249  
250  
251  
252  
253  
254  
255  
256  
257  
258  
259  
260  
261  
262  
263  
264  
265  
266  
267  
268  
269  
270  
271  
272  
273  
274  
275  
276  
277  
278  
279  
280  
281  
282  
283  
284  
285  
286  
287  
288  
289  
290  
291  
292  
293  
294  
295  
296  
297  
298  
299  
300  
301  
302  
303  
304  
305  
306  
307  
308  
309  
310  
311  
312  
313  
314  
315  
316  
317  
318  
319  
320  
321  
322  
323  
324  
325  
326  
327  
328  
329  
330  
331  
332  
333  
334  
335  
336  
337  
338  
339  
340  
341  
342  
343  
344  
345  
346  
347  
348  
349  
350  
351  
352  
353  
354  
355  
356  
357  
358  
359  
360  
361  
362  
363  
364  
365  
366  
367  
368  
369  
370  
371  
372  
373  
374  
375  
376  
377  
378  
379  
380  
381  
382  
383  
384  
385  
386  
387  
388  
389  
390  
391  
392  
393  
394  
395  
396  
397  
398  
399  
400  
401  
402  
403  
404  
405  
406  
407  
408  
409  
410  
411  
412  
413  
414  
415  
416  
417  
418  
419  
420  
421  
422  
423  
424  
425  
426  
427  
428  
429  
430  
431  
432  
433  
434  
435  
436  
437  
438  
439  
440  
441  
442  
443  
444  
445  
446  
447  
448  
449  
450  
451  
452  
453  
454  
455  
456  
457  
458  
459  
460  
461  
462  
463  
464  
465  
466  
467  
468  
469  
470  
471  
472  
473  
474  
475  
476  
477  
478  
479  
480  
481  
482  
483  
484  
485  
486  
487  
488  
489  
490  
491  
492  
493  
494  
495  
496  
497  
498  
499  
500  
501  
502  
503  
504  
505  
506  
507  
508  
509  
510  
511  
512  
513  
514  
515  
516  
517  
518  
519  
520  
521  
522  
523  
524  
525  
526  
527  
528  
529  
530  
531  
532  
533  
534  
535  
536  
537  
538  
539  
540  
541  
542  
543  
544  
545  
546  
547  
548  
549  
550  
551  
552  
553  
554  
555  
556  
557  
558  
559  
560  
561  
562  
563  
564  
565  
566  
567  
568  
569  
570  
571  
572  
573  
574  
575  
576  
577  
578  
579  
580  
581  
582  
583  
584  
585  
586  
587  
588  
589  
590  
591  
592  
593  
594  
595  
596  
597  
598  
599  
600  
601  
602  
603  
604  
605  
606  
607  
608  
609  
610  
611  
612  
613  
614  
615  
616  
617  
618  
619  
620  
621  
622  
623  
624  
625  
626  
627  
628  
629  
630  
631  
632  
633  
634  
635  
636  
637  
638  
639  
640  
641  
642  
643  
644  
645  
646  
647  
648  
649  
650  
651  
652  
653  
654  
655  
656  
657  
658  
659  
660  
661  
662  
663  
664  
665  
666  
667  
668  
669  
670  
671  
672  
673  
674  
675  
676  
677  
678  
679  
680  
681  
682  
683  
684  
685  
686  
687  
688  
689  
690  
691  
692  
693  
694  
695  
696  
697  
698  
699  
700  
701  
702  
703  
704  
705  
706  
707  
708  
709  
710  
711  
712  
713  
714  
715  
716  
717  
718  
719  
720  
721  
722  
723  
724  
725  
726  
727  
728  
729  
730  
731  
732  
733  
734  
735  
736  
737  
738  
739  
740  
741  
742  
743  
744  
745  
746  
747  
748  
749  
750  
751  
752  
753  
754  
755  
756  
757  
758  
759  
760  
761  
762  
763  
764  
765  
766  
767  
768  
769  
770  
771  
772  
773  
774  
775  
776  
777  
778  
779  
780  
781  
782  
783  
784  
785  
786  
787  
788  
789  
790  
791  
792  
793  
794  
795  
796  
797  
798  
799  
800  
801  
802  
803  
804  
805  
806  
807  
808  
809  
810  
811  
812  
813  
814  
815  
816  
817  
818  
819  
820  
821  
822  
823  
824  
825  
826  
827  
828  
829  
830  
831  
832  
833  
834  
835  
836  
837  
838  
839  
840  
841  
842  
843  
844  
845  
846  
847  
848  
849  
850  
851  
852  
853  
854  
855  
856  
857  
858  
859  
860  
861  
862  
863  
864  
865  
866  
867  
868  
869  
870  
871  
872  
873  
874  
875  
876  
877  
878  
879  
880  
881  
882  
883  
884  
885  
886  
887  
888  
889  
890  
891  
892  
893  
894  
895  
896  
897  
898  
899  
900  
901  
902  
903  
904  
905  
906  
907  
908  
909  
910  
911  
912  
913  
914  
915  
916  
917  
918  
919  
920  
921  
922  
923  
924  
925  
926  
927  
928  
929  
930  
931  
932  
933  
934  
935  
936  
937  
938  
939  
940  
941  
942  
943  
944  
945  
946  
947  
948  
949  
950  
951  
952  
953  
954  
955  
956  
957  
958  
959  
960  
961  
962  
963  
964  
965  
966  
967  
968  
969  
970  
971  
972  
973  
974  
975  
976  
977  
978  
979  
980  
981  
982  
983  
984  
985  
986  
987  
988  
989  
990  
991  
992  
993  
994  
995  
996  
997  
998  
999  
1000

1  
2  
3 Each calibration data set Hyperion acquired the RVPN test sites on slightly  
4 different portions of the Hyperion focal plane. A summary of focal plane coverage is  
5 shown in Figure 1a where the horizontal axis is Hyperion's spatial column and vertical  
6 axis is the date of the collection. Recall that each pixel of Hyperion has a unique spectral  
7 response function defined by a band center and bandwidth of a gaussian curve. The band  
8 center wavelength is slowly varying across the focal plane for a given spectral channel  
9 and the variation is nearly negligible for a four-to-eight pixel-sized test site. Figure 1b  
10 shows the maximum band center change across the field of a test site for the VNIR and  
11 SWIR focal planes. The band center changes from one data set to another is more  
12 significant and as much as 0.5 nm between the extremes as shown in Figure 1c. Therefore,  
13 the approach used to band average predicted at-sensor radiance is to use the average band  
14 center and bandwidth for each data set.  
15  
16  
17  
18  
19  
20  
21  
22  
23  
24  
25  
26  
27  
28  
29  
30

31  
32 The dates and times of each Hyperion acquisition used in this work are listed in  
33 Table I. The corresponding surface reflectance measurement time, test site layout, solar  
34 and sensor geometries, and atmospheric parameters are listed for each overpass. The  
35 surface reflectance of the test site was typically measured over a 30–40 minute period  
36 during which the solar zenith has a nominal change of about five degrees. Most of the  
37 data sets have a high solar zenith angle in the range of 25–30 degrees except for two  
38 winter data sets having solar zenith angle of 45 and 50 degrees. The reflectance-based  
39 method is insensitive to these differences because surface reflectance is characterized  
40 with the ground-based instrumentation in nearly the same view and illumination  
41 geometry as Hyperion.  
42  
43  
44  
45  
46  
47  
48  
49  
50  
51  
52  
53  
54  
55  
56  
57  
58  
59  
60

1  
2  
3 The solid line in Figure 2 shows surface spectral reflectance of the 120 × 480 m  
4 site at RVPN as measured on 5 March 2005 and the dashed line shows the percent  
5 standard deviation of the mean. The reflectance curve is typical of RVPN and very  
6 similar to the other data sets. The standard deviation represents a combination of  
7 measurement noise and test site variability. The variability shown for 5 March 2005 of  
8 about 5% in most spectral regions is the highest of the ten data sets used in this work and  
9 most are in the range of 2–4%. The peaks in standard deviation near 1400 and 1800 nm  
10 are due to low signal levels caused absorption due to water vapor. The 2300–2500 nm  
11 spectral region also experiences significant variability due to decreasing signal level and  
12 increasing instrument noise.  
13  
14  
15  
16  
17  
18  
19  
20  
21  
22  
23  
24  
25  
26

27 The measured surface reflectance and corresponding atmospheric parameters are  
28 used to constrain the radiative transfer code to predict at-sensor radiance which has an  
29 output with higher spectral resolution than the Hyperion bands. The spectral radiance  
30 curve from the radiative transfer code is band averaged with the appropriate spectral  
31 response functions that depend on the spatial location on the focal plane where the test  
32 site is imaged. The results are presented as percent disagreement between the at-sensor  
33 radiance prediction and radiance reported by the current calibration of Hyperion.  
34  
35  
36  
37  
38  
39  
40  
41  
42  
43

$$44 \quad \% \text{ difference} = \frac{L_{\text{predicted}, \lambda} - L_{\text{Hyperion}, \lambda}}{L_{\text{predicted}, \lambda}}$$

45  
46

47 where  $L_{\text{predicted}, \lambda}$  and  $L_{\text{Hyperion}, \lambda}$  are the spectral radiance values from the reflectance-based  
48 approach and Hyperion, respectively. The averaged % difference results from the nine  
49 field campaigns are shown in Figure 3. Spectral regions of large deviation from zero,  
50 such as 940, 1130, 1350 and 2400 nm, are affected by strong water vapor absorption. A  
51 combination of lower signal for both Hyperion and the ground-based spectrometer  
52  
53  
54  
55  
56  
57  
58  
59  
60

1  
2  
3 coupled with high sensitivity to atmospheric characterization in these spectral regions  
4  
5 leads to unreliable results. The remainder of the data in Figure 3 shows agreement  
6  
7 between Hyperion and reflectance-based results to within -5% and +10%. A convenient  
8  
9 way to assess the consistency of these results is to find the standard deviation of the mean  
10  
11 as shown in Figure 4. Excluding the high variability of the previously mentioned spectral  
12  
13 regions affected by water vapor absorption, the consistency for the reflectance-based  
14  
15 method is on the 2% level. The band-to-band consistency of the standard deviation  
16  
17 indicates that band-to-band variability in the percent differences are real effects caused by  
18  
19 the calibration of Hyperion. The implication of these results is that a smoothly varying  
20  
21 spectral radiance would display band-to-band variations on the order of 5–10% simply  
22  
23 because of the radiometric calibration of the system.  
24  
25  
26  
27  
28

29 The results shown here for Hyperion compare favorably in standard deviation to  
30  
31 those derived for other sensors (Thome, 2001; Thome et al., 2003, McCorkel et al., 2006).  
32  
33 Such favorable comparisons give confidence in the results for Hyperion. Additionally,  
34  
35 each of the nine dates shown also included calibration attempts for other sensors using  
36  
37 the ground data collected for Hyperion or using data sets collected near in time and  
38  
39 location for other sensors. The results for the other sensors are consistent with long-term  
40  
41 trends for those instruments (such as Landsat-5 Thematic Mapper and Landsat 7  
42  
43 Enhanced Thematic Mapper Plus). The internal consistency of the reflectance-based  
44  
45 results with other dates and imagers gives good confidence in the average percent  
46  
47 difference shown for Hyperion.  
48  
49  
50  
51  
52

53 Reflectance-based results for Hyperion cover the 2001–2005 period, concurrent  
54  
55 with less than half of Hyperion's lifetime, means that they can not provide the exclusive  
56  
57  
58  
59  
60

1  
2  
3 calibration. This work uses reference to the moon to show that the reflectance-based  
4  
5 results presented above remain valid through the mission. The black lines in Figure 5  
6  
7 show the changes in Hyperion response over the past 11 years as deduced by the ROLO  
8  
9 normalized measurements. The comparison to ROLO is shown for six channels, three for  
10  
11 the each of Hyperion's focal planes. The red lines in Figure 5 are linear best fits to  
12  
13 ROLO-based results and the associated annual degradation rates are shown in Table II.  
14  
15 All channels presented here show 0.1%/year or less rate of change except for channel 11  
16  
17 with band center at 457 nm.  
18  
19

20  
21  
22 The blue circles in Figure 5 show the reflectance-based results for the same  
23  
24 spectral channels. The average values with associated percent standard deviation and  
25  
26 rates of change are shown in Table II. There is limited confidence in these degradation  
27  
28 rates due to the relatively small number of data points and 2% relative uncertainty. The  
29  
30 primary differences in these data sets other than the temporal coverage discussed above  
31  
32 are significant absolute differences and larger scatter in the reflectance-based results. The  
33  
34 amount of variability in the reflectance-based data set is expected due primarily to  
35  
36 uncertainties in the reflectance retrieval. The absolute uncertainty of the reflectance-  
37  
38 based method has been shown to be <3% for the spectral bands shown here (Thome et al.,  
39  
40 2005). The absolute uncertainty in the knowledge of the lunar calibration is 5–10%  
41  
42 (Stone and Kieffer, 2006). Thus, the results shown in the figures technically overlap in an  
43  
44 absolute sense.  
45  
46  
47  
48  
49

50  
51 The true power of the lunar results shown are that they cover a much longer time  
52  
53 period than the reflectance-based results and the better precision of the lunar data allows  
54  
55 for greater confidence in the trend of the calibration of Hyperion. The results for the 457-  
56  
57  
58  
59  
60



1  
2  
3 nm band are still being evaluated to determine if the small change in response over the 10  
4 years of Hyperion operation is real. Results for the other bands show very good stability  
5  
6 for the Hyperion sensor for the lifetime of the instrument. Knowledge of the stability of  
7  
8 the Hyperion calibration allows for an average absolute calibration based on the  
9  
10 reflectance-based results to be determined and applicable for the lifetime of Hyperion.  
11  
12  
13  
14  
15  
16  
17  
18  
19  
20  
21  
22  
23

## 24 **V. Conclusion**

25  
26  
27  
28  
29 Nine vicarious calibration campaigns consisting of ground-based reflectance and  
30 atmospheric measurements, known as the reflectance-based approach, during 2001–2005  
31 were held for the Hyperion imaging spectrometer. Disagreement between spectral  
32 radiance predicted with the reflectance-based approach and that measured by Hyperion  
33 ranges -5–10% depending on spectral region. The variability of these results are on the  
34  
35 2% level based on the standard deviation of the nine data sets for most spectral channels  
36  
37 of Hyperion.  
38  
39  
40  
41  
42  
43  
44  
45

46 The absolute calibration of the reflectance-based approach is complemented by  
47 the more frequent, continuous, and precise characterization provided by lunar  
48 acquisitions tied to the ROLO model. Lunar images were acquired at least every two  
49 months and the irradiance from the moon is calculated and compared with that calculated  
50 from the ROLO model. ROLO-based results have about one quarter of the variability of  
51  
52  
53  
54  
55  
56  
57  
58  
59  
60

1  
2  
3 the reflectance-based calibration data set. The stability shown with the lunar data set  
4  
5 gives confidence that the absolute calibration of the reflectance-based approach is valid  
6  
7 throughout the lifetime of the sensor. Such results should be used to improve the band-to-  
8  
9 band calibration of the Hyperion sensor to remove effects that cause spectral variability  
10  
11 in retrieved surface reflectance.  
12  
13

14  
15 Such a band-to-band radiometric calibration is not trivial due to the variation in  
16  
17 spectral bandpass and center wavelength across the Hyperion swath. The work shown  
18  
19 here relies sampling a relatively small portion of Hyperion's spatial swath due to the  
20  
21 focal plane location where the RVPN was typically imaged. Therefore these results rely  
22  
23 on the quality of the flat field knowledge of the sensor and future work with large and  
24  
25 more uniform and stable test sites will increase confidence and should allow a band-to-  
26  
27 band radiometric calibration of Hyperion. Improved understanding of the absolute  
28  
29 radiometric calibration of each Hyperion band will greatly improve the utility of  
30  
31 Hyperion data for many applications. As an example, the calibration found here can be  
32  
33 used to better characterize the reflectance curve of remote desert test sites that are not  
34  
35 accessible for groundwork and these test sites will be used to improve the intercalibration  
36  
37 understanding of a wide range of sensors.  
38  
39  
40  
41  
42  
43  
44  
45  
46  
47  
48  
49  
50  
51  
52  
53  
54  
55  
56  
57  
58  
59  
60

## REFERENCES

1  
2  
3  
4  
5  
6  
7  
8  
9  
10  
11  
12  
13  
14  
15  
16  
17  
18  
19  
20  
21  
22  
23  
24  
25  
26  
27  
28  
29  
30  
31  
32  
33  
34  
35  
36  
37  
38  
39  
40  
41  
42  
43  
44  
45  
46  
47  
48  
49  
50  
51  
52  
53  
54  
55  
56  
57  
58  
59  
60

Ångström, A., "On the atmospheric transmission of sun radiation and on dust in the air," *Geografiska Annaler*, Vol. 11, pp. 156-166, 1929.

Arai, K., Tonooka, H., "Radiometric performance evaluation of ASTER VNIR, SWIR, and TIR," *IEEE Transactions of Geoscience and Remote Sensing* 43(12), 2725-2732 (2005).

Barnes, R. A., R. E. Eplee, Jr., G. M. Schmidt, F. S. Patt, and C. R. McClain, "Calibration of SeaWiFS. I. Direct Techniques," *Applied Optics*, 40, pp. 6682-6700, 2001.

Berk, A., L.S. Bernstein, and D.C. Robertson, "MODTRAN: A Moderate Resolution Model for LOWTRAN," Air Force Geophysics Laboratory, Air Force Systems Command, Hanscom AFB, Massachusetts, 1987.

Berk, A., L.S. Bernstein, G.P. Anderson, P.K. Acharya, D.C. Robertson, J.H. Chetwynd, S.M. Adler-Golden, "MODTRAN cloud and multiple scattering upgrade with application to AVIRIS," *Remote Sensing of Environment* 65(3), 367-375 (1998).

Biggar, S.F., Labeled, J. F., Santer, R. P., Slater, P. N., Jackson, R. D., and Moran, M. S., "Laboratory calibration of field reflectance panels," *Proc. SPIE* 924, 232-240 (1988).

Biggar, S.F., "Improved evaluation of optical depth components from Langley plot data," *Remote Sensing of Environment*, Vol. 32, No. 2-3, pp. 91-101, 1990.

Biggar, S. F., K. J. Thome, W. T. Wisniewski, "Vicarious radiometric calibration of EO-1 sensors by reference to high-reflectance ground targets," *IEEE Trans. On Geosciences and Remote Sensing*, 41, pp. 1174-1179, 2003.

Gellman, D. I., Biggar, S. F., Slater, P. N., & Bruegge, C. J. (1991). Calibrated intercepts for solar radiometers used in remote sensor calibration. *Proceedings of SPIE*, 1493, 175-180.

Kieffer, H.H., R.L. Wildey, "Establishing the Moon as a Spectral Radiance Standard", *J. Atmospheric and Oceanic Technology* 13, 2, 360-375 (1996)

Kieffer, H.H., T.C. Stone, "The Spectral Irradiance of the Moon", *Astronom. J.* 129, 2887-2901 (2005)

McCorkel, J.T., K.T. Thome, S.F. Biggar, M.J. Kuester, "Radiometric Calibration of Advanced Land Imager using reflectance-based results between 2001 and 2005," *Proceedings of SPIE*, Vol. 6296, 2006.

1  
2  
3  
4  
5  
6  
7  
8  
9  
10  
11  
12  
13  
14  
15  
16  
17  
18  
19  
20  
21  
22  
23  
24  
25  
26  
27  
28  
29  
30  
31  
32  
33  
34  
35  
36  
37  
38  
39  
40  
41  
42  
43  
44  
45  
46  
47  
48  
49  
50  
51  
52  
53  
54  
55  
56  
57  
58  
59  
60

McPeters, R. D., Bhartia, P. K., Krueger, A. J., Herman, J. R., Wellemeyer, C. G., Seftor, C. J., Jaross, G., Torres, O., Moy, L., Labow, G., Byerly, W., Taylor, S. L., Swissler, T., & Cebula Raytheon, R. P. (1998). Earth probe total ozone mapping spectrometer (TOMS) data product user's guide (NASA Technical Publication, 1998-206895). National Aeronautics and Space Administration. Washington, DC, USA.

Penndorf, R., "Tables of the Refractive Index for Standard Air and the Rayleigh Scattering Coefficient for the Spectral Region between 0.2 and 20.0  $\mu$  and Their Application to Atmospheric Optics," *Journal of the Optical Society of America*, 47 (2), 1957.

Reagan, J.A. K.J. Thome, B.M. Herman, "A simple instrument and technique for measuring columnar water vapor via near-IR differential solar transmission measurements," *IEEE Trans. Geosci. Rem. Sens.*, Vol. 30, No. 4, pp. 825-831, 1992.

Scott, K. P., Thome, K. J., Brownlee, M. R., "Evaluation of the Railroad Valley playa for use in vicarious calibration," *Proc. SPIE* 2818, 158-166 (1996).

Stone, T. C., H. H. Kieffer, and K. J. Becker, "Modeling the Radiance of the Moon for On-orbit Calibration", *Proc. SPIE* **5151**, 463-470 (2003)

Stone, T.C., H.H. Kieffer, "Assessment of Uncertainty in ROLO Lunar Irradiance for On-orbit Calibration", *Proc. SPIE* 5542, 300-310 (2004)

Stone, T.C., H. H. Kieffer, "Use of the Moon to support onorbit sensor calibration for climate change measurements," *Proc. SPIE* 6296, 62960Y (2006)

Teillet, P.M., "Rayleigh optical depth comparisons from various sources," *Applied Optics*, 29 (13), 1897-1900, 1990.

Thome, K.J., "Absolute radiometric calibration of Landsat 7 ETM+ using the reflectance-based method," *Remote Sensing of Environment*, Vol. 78, No. 1, pp. 27-38, 2001.

Thome, K.J., E.E. Whittington, and N. Smith, "Radiometric calibration of MODIS with reference to Landsat-7 ETM+," *Proceedings of SPIE*, Vol. 4483, pp. 203-210, 2003.

Thome, K., S. Biggar, and H. J. Choi, "Vicarious calibration of Terra ASTER, MISR, and MODIS," *Proc. SPIE Conf. #5542*, pp. 290-299, Denver, Colo., 2004a.

Thome, K. J., Helder, D. L., Aaron, D., Dewald, J. D., "Landsat-5 TM and Landsat-7 ETM+ Absolute Radiometric Calibration Using the Reflectance-Based Method," *IEEE Transactions of Geoscience and Remote Sensing* 42(12), 2777-2785, 2004b.

Thome, K., C. Cattrell, J. D'Amico, J. Geis, "Ground-reference calibration results for Landsat 7 ETM+," *Proceedings of SPIE*, Vol. 5882, 2005.

1  
2  
3 Vane, G., Green, R. O., Chrien, T. G., Enmark, H. T., Hansen, E. G., Porter, W. M., "The  
4 Airborne Visible/Infrared Imaging Spectrometer (AVIRIS)," Remote Sensing of  
5 Environment 44, 127-143 (1993).  
6  
7

8 Veefkind, J. P., de Haan, J. F., Brinksma, E. J., Kroon, M., Levelt, P. F., "Total ozone  
9 from the ozone monitoring instrument (OMI) using the DOAS technique," IEEE  
10 Transactions of Geoscience and Remote Sensing 44(5), 1239- 1244 (2006).  
11  
12  
13  
14  
15  
16  
17  
18  
19  
20  
21  
22  
23  
24  
25  
26  
27  
28  
29  
30  
31  
32  
33  
34  
35  
36  
37  
38  
39  
40  
41  
42  
43  
44  
45  
46  
47  
48  
49  
50  
51  
52  
53  
54  
55  
56  
57  
58  
59  
60

For Review Only

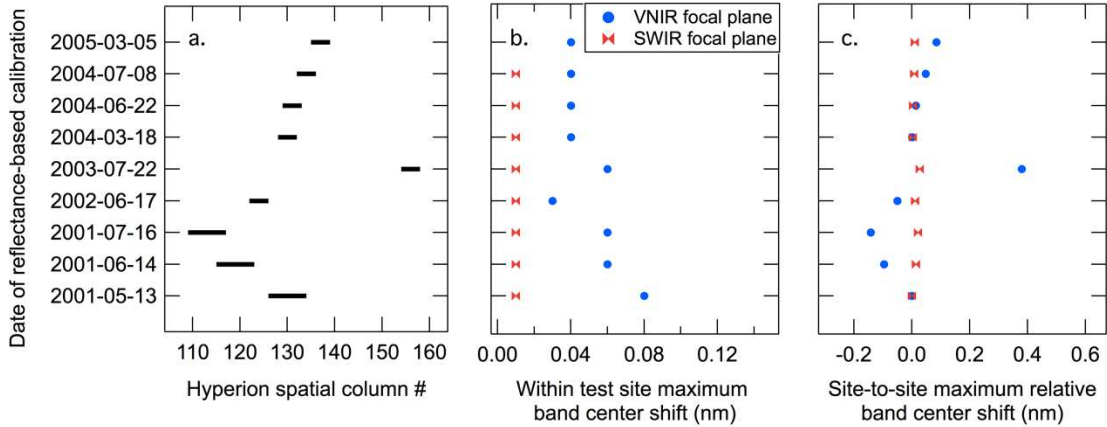


Fig. 1. Spatial and spectral attributes for each calibration data point including a) Hyperion spatial columns covered by RVPN test site for each data set, b) maximum spectral offset of band center values within data sets, and c) maximum spectral offset of band center values amongst data sets relative to the first.

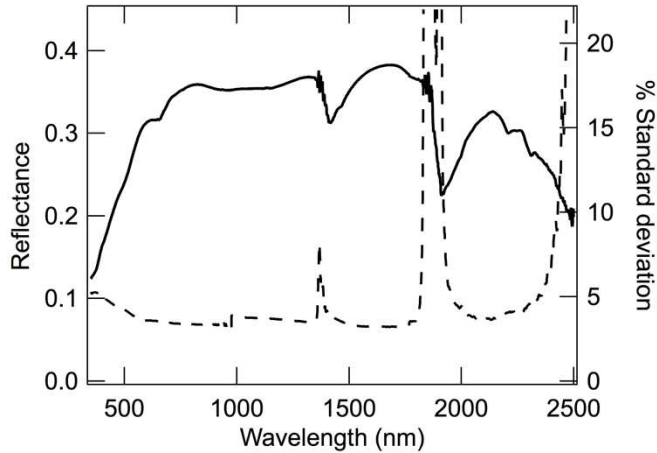


Fig. 2. Spectral reflectance of RVPN measured on 5 March 2005.

1  
2  
3  
4  
5  
6  
7  
8  
9  
10  
11  
12  
13  
14  
15  
16  
17  
18  
19  
20  
21  
22  
23  
24  
25  
26  
27  
28  
29  
30  
31  
32  
33  
34  
35  
36  
37  
38  
39  
40  
41  
42  
43  
44  
45  
46  
47  
48  
49  
50  
51  
52  
53  
54  
55  
56  
57  
58  
59  
60

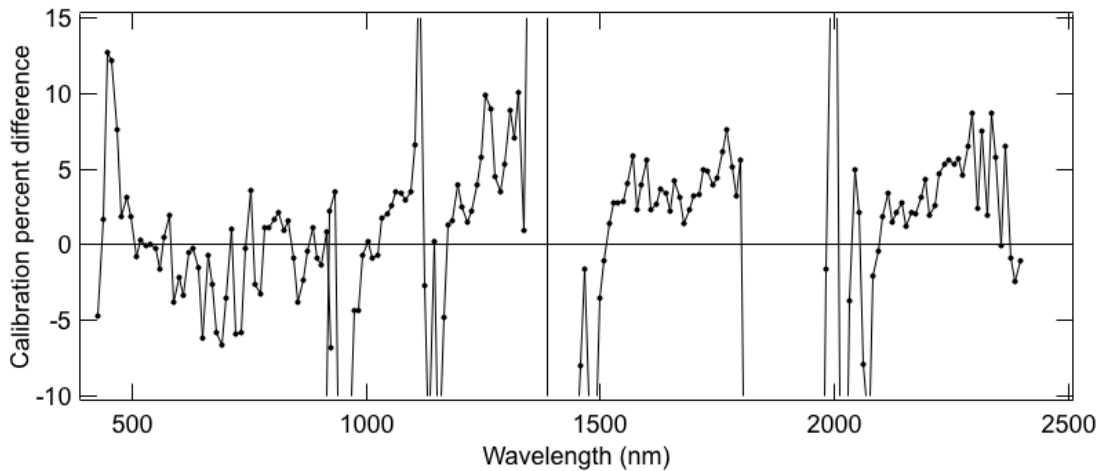


Fig. 3. Mean of nine data sets in the form of percent disagreement between at-sensor radiance prediction and the current calibration of Hyperion.

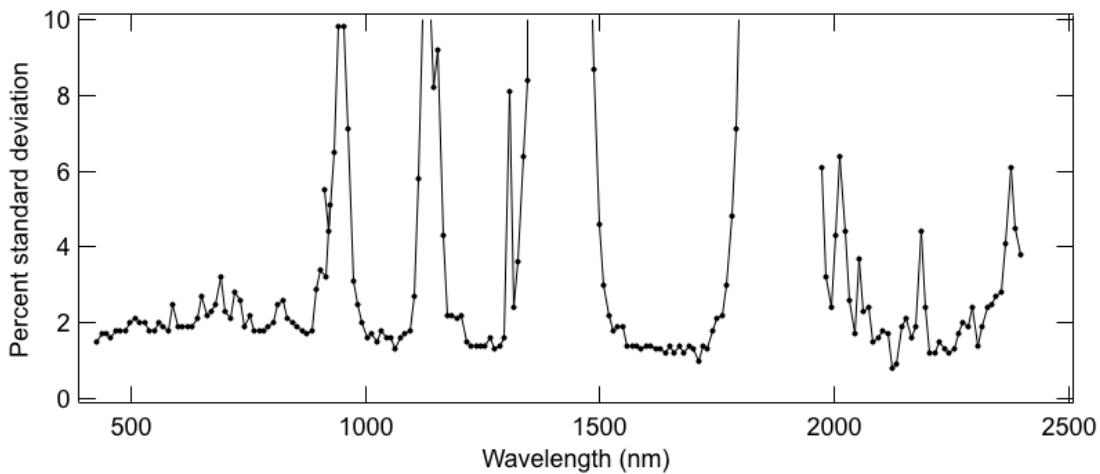


Fig. 4. Percent standard deviation of the mean disagreement between at-sensor radiance prediction and the current calibration of Hyperion.

1  
2  
3  
4  
5  
6  
7  
8  
9  
10  
11  
12  
13  
14  
15  
16  
17  
18  
19  
20  
21  
22  
23  
24  
25  
26  
27  
28  
29  
30  
31  
32  
33  
34  
35  
36  
37  
38  
39  
40  
41  
42  
43  
44  
45  
46  
47  
48  
49  
50  
51  
52  
53  
54  
55  
56  
57  
58  
59  
60

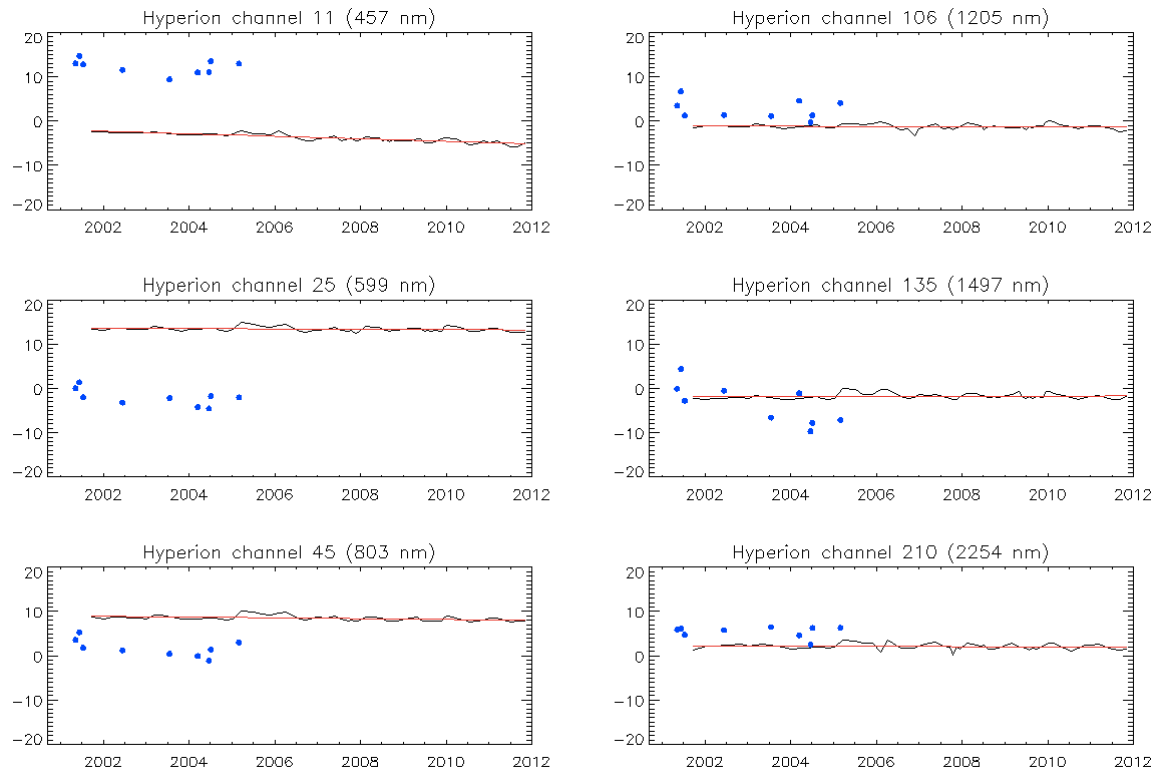


Fig. 5. Hyperion percent difference from the ROLO model and reflectance-based results for three channels each of Hyperion's focal planes.

Table I. Summary of measurement data for the nine Hyperion acquisitions of RVPN with coincident ground collections.

Acquisition date	13 May 2001	14 June 2001	16 July 2001	17 June 2002	22 July 2003	18 March 2004	22 June 2004	8 July 2004	5 March 2005
Acquisition time (UTC)	18:12:04	18:11:40	18:11:24	18:10:34	18:10:37	18:11:20	18:11:10	18:10:59	18:11:50
Surface refl time (UTC)	18:13-18:42	17:50-18:22	17:40-18:23	17:33-18:10	17:46-17:53	17:45-18:22	17:37-18:15	17:35-18:11	17:36-18:14
Solar zenith range	27.2-23.4	28.3-22.8	32.5-25.1	31.4-24.9	32.1-30.8	48.5-43.9	31.0-24.3	32.6-26.1	54.6-49.9
Test site layout (m)	90 × 240	90 × 240	90 × 240	120 × 480	120 × 480	120 × 480	120 × 480	120 × 480	120 × 480
Solar zenith	27.4	24.6	27.0	24.8	28.0	45.3	24.9	26.1	50.4
Solar azimuth	130.6	121.6	122.8	120.8	123.6	143.8	120.6	121.3	146.0
View zenith	1.6	1.4	1.5	1.3	0.3	1.4	1.3	1.3	0.1
View azimuth	98.2	98.2	98.2	98.2	103.0	98.2	98.2	98.2	105.0
Temperature (°C)	32	13	30	34	39	19	30	33	13
Pressure (mb)	858	855	851	856	859	859	857	854	860
Angstrom parameter	1.16	1.68	0.35	1.12	1.42	0.90	2.18	1.03	0.66
Water vapor (cm)	1.36	0.53	0.77	0.56	2.48	0.76	1.47	1.71	0.91
Aerosol optical depth @ 550 nm	0.073	0.032	0.040	0.110	0.097	0.075	0.095	0.089	0.038
Ozone (DU)	308	311	328	303	280	313	296	299	308



Table II. Summary of ROLO model-based comparison to Hyperion with associated reflectance-based results.

Hyperion channel	Band center	Mean percent difference from Hyperion radiance		Percent standard deviation		% change/year	
		Refl-based	ROLO-based	Refl-based	ROLO-based	Refl-based	ROLO-based
11	457	12.15	-3.87	1.60	0.90	-0.37	-0.28
25	599	-2.15	13.39	1.87	0.52	-0.77	-0.04
45	803	1.64	8.43	1.98	0.57	-0.73	-0.09
106	1205	2.54	-1.23	2.21	0.59	-0.36	-0.02
135	1497	-3.56	-1.75	4.60	0.63	-2.36	0.01
210	2254	5.33	2.08	1.27	0.65	-0.14	-0.04

For Review Only

1  
2  
3  
4  
5  
6  
7  
8  
9  
10  
11  
12  
13  
14  
15  
16  
17  
18  
19  
20  
21  
22  
23  
24  
25  
26  
27  
28  
29  
30  
31  
32  
33  
34  
35  
36  
37  
38  
39  
40  
41  
42  
43  
44  
45  
46  
47  
48  
49  
50  
51  
52  
53  
54  
55  
56  
57  
58  
59  
60



**Joel McCorkel** received a BS degree in Optical Engineering and PhD in Optical Sciences from the University of Arizona. He joined the National Ecological Observatory Network as a staff scientist for the Airborne Observation Platform in 2009. He is currently a physical scientist in the Biospheric Sciences Laboratory at NASA's Goddard Space Flight Center, Greenbelt, Maryland.



**Kurt Thome** obtained a BS degree in meteorology from Texas A&M University and MS and PhD degrees in atmospheric sciences from the University of Arizona. He then joined what is now the College of Optical Sciences becoming full professor in 2006. He served as the Director of the Remote Sensing Group from 1997 to 2008. Thome moved to NASA's Goddard Space Flight Center in 2008 as a Physical Scientist in the Biospheric Sciences Laboratory. He has been a member of the Landsat-7, ASTER, MODIS, and EO-1 Science Teams providing vicarious calibration results for those and other imaging sensors. He is a Fellow of SPIE, is the Instrument Scientist for the Visible Infrared Imaging Radiometer Suite on the Joint Polar Satellite System and is serving as the calibration lead for the Thermal Infrared Sensor on the Landsat Data Continuity Mission. Thome is the Deputy Project Scientist for CLARREO for which he is also the instrument lead for the Reflected Solar Instrument.

**Lawrence Ong**